Nano Today 57 (2024) 102332

Contents lists available at ScienceDirect

Nano Today

journal homepage: www.elsevier.com/locate/nanotoday

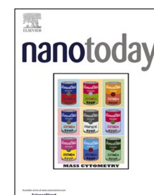

Two-dimensional materials based volatile memristors mediated by flexoelectric effect

Menghan Deng [a], Zhaotan Gao [a], Lin Wang [a], Zhangchen Hou [a], Xionghu Xu [a], Li Chen [a], Anyang Cui [a], Kai Jiang [a], Liyan Shang [a], Liangqing Zhu [a], Yawei Li [a], Jinzhong Zhang [a,*], Zhigao Hu [a,b,*]

[a] Technical Center for Multifunctional Magneto-Optical Spectroscopy (Shanghai), Engineering Research Center of Nanophotonics & Advanced Instrument (Ministry of Education), Department of Physics, School of Physics and Electronic Science, East China Normal University, Shanghai 200241, China
[b] Collaborative Innovation Center of Extreme Optics, Shanxi University, Taiyuan, Shanxi 030006, China

ARTICLE INFO

Keywords:
Van der Waals layered materials
Flexoelectric effect
Volatile memristor
Multi-field perception
Artificial nociceptor

ABSTRACT

The study of conventional lateral memristors has been in a slow stage of development due to the dependence of the atomic defect migration or local phase transition in two-dimensional (2D) materials. Here, a novel transversal memristor based on the flexoelectric effect induced by a bent atomic laminated structure is proposed. The memristor exhibits desirable resistive switching performance, including a current ON/OFF ratio of approximately 10^5, forming-free operation, high yield of 97 %, and low cycle-to-cycle variation of only 7.4 %. The stable analog memristive behavior could be attributed to the dynamic modulation of the barrier between suspended and flat regions by external voltage biases. Further, the volatile resistance switching characteristics have successfully emulated key features of multi-field perceptual artificial nociceptors, including threshold, "no adaptation" etc. This work demonstrates a new resistive switching phenomenon in transversal 2D material devices, and opens a new way for the development of intelligent adaptive artificial sensory systems.

Introduction

Over the past decades, with the rapid development of the Big Data and Internet of Things (IoT) era, the amount of data processed by information about mobile edge devices has exploded. [1] The exponential growth of data information requires memristors to have the advantages of large capacity, low power consumption, high dependence, fast writing/erasing speed, etc. However, three-dimensional (3D) oxide materials are difficult to reduce the compression size and cannot be used in superintegrated and ultrahigh-capacity memristors. Due to the downscaling limitations of traditional oxide materials, two-dimensional (2D) layered materials as platforms for low-power and high-performance memristors have garnered significant attention in recent times. [2] Memristors on the basis of 2D layered materials could be classified into two categories according to their geometric structure, namely, lateral- and vertical-structures. [3,4] In contrast to conventional two-terminal vertical structures, 2D material-based lateral devices can achieve electrostatic gate tunability [5] and multi-terminal structures. [6,7] They have a similar structure with conventional field-effect transistors (FETs), [8] generally consisting of horizontal arrangement metal electrodes and transition metal dichalcogenides channels on dielectric substrates, with current flowing along the in-plane direction. Therefore, lateral memristors could be used as a device platform to simulate the multi-terminal neuromorphic circuit with multiple synaptic links in biological neurons for complex learning with high energy efficiency.

Recently, 2D materials-based lateral memristors have been preliminarily explored. Sangwan *et al.* reported lateral polycrystalline monolayer MoS_2 memristors for the first time in 2015. The migration of sulfur vacancies at grain boundaries is the reason for the identified memristive states. It presents that the memristive and dynamic negative differential resistance characteristics only exist in monolayer MoS_2 memristors with intersecting grain boundaries. [6] A monolayer of polycrystalline MoS_2

* Corresponding author.
* Corresponding author at: Technical Center for Multifunctional Magneto-Optical Spectroscopy (Shanghai), Engineering Research Center of Nanophotonics & Advanced Instrument (Ministry of Education), Department of Physics, School of Physics and Electronic Science, East China Normal University, Shanghai 200241, China.
E-mail addresses: jzzhang@ee.ecnu.edu.cn (J. Zhang), zghu@ee.ecnu.edu.cn (Z. Hu).

https://doi.org/10.1016/j.nantod.2024.102332
Received 26 March 2024; Received in revised form 26 May 2024; Accepted 29 May 2024
1748-0132/© 2024 Elsevier Ltd. All rights are reserved, including those for text and data mining, AI training, and similar technologies.

was then incorporated into a memtransistor, which was fabricated as a Schottky barrier transistor and can be altered dynamically through the application of external voltage biases. [7] Except for the defect-mediated memristive behavior in 2D materials, the phase transition behavior is also one of the reasons for the unusual memristive switching behavior. Lu *et al.* reported a MoS_2 phase transition memristor that induces the reversible modulation between 2 H (semiconductor) and 1 T′ (metal) phases of MoS_2 nano-sheets by controlling the migration of Li^+ ions. [9] Furthermore, the 1 T-phase TaS_2 memristors are activated by the phase transition in the charge density wave, which are created by the periodic lattice distortion. [10] At present, the construction of 2D material-based lateral memristors requires the introduction of atomic defects or the selection of 2D materials with phase transition properties as channel materials, which have certain requirements of the materials themselves. Since the strong reliance on defects and phase transition behavior, the relevant study of 2D material-based planar memristors has been in a slow stage of development. However, a scalable, reproducible, and controllable manufacturing method is a prerequisite for the introduction of lateral memristors into industrial applications. Therefore, we especially expect a reliable approach to construct planar memristors that avoids the certain requirements of traditional lateral memristor on 2D material.

In this work, taking InSe flakes with innate ultrahigh mobility and hypersensitivity to light as a representative of 2D layered materials, [11] we have creatively put forward a general strategy for constructing lateral memristors. The unique layered structure of suspended atomic is designed to produce flexoelectric effect on bent 2D InSe sheets. It is found that the memristor exhibits outstanding resistive switching characteristics, including a large ON/OFF ratio around 10^5, forming-free operation, up to 97 % yield, and cycle-to-cycle variation of 7.4 %. Compared to the flat InSe (F-InSe) area, the surface potential of the suspended InSe (S-InSe) region decreases significantly, which originates primarily from the raising of work function resulting from the non-uniform strain. The deviations in surface potential between suspended and flat InSe regions lead to the existence of barriers. The dynamic modulation of the barrier by applying external biases determines the stable analog resistive switching behavior of the InSe-based memristors. Finally, the volatile memristive behavior successfully simulates key features of artificial nociceptors under multi-field (light and electric field) perception, including threshold, relaxation, “no adaptation” and sensitization. This work provides a new idea for 2D-based lateral memristors, and establishes a new path for the design of artificial sensory systems with intelligent adaptability.

Results and discussion

Flexoelectric polarization and memristive behavior

Fig. 1a shows the experimental schematics of scanning probe microscopy (SPM)-based piezoresponse force microscopy (PFM) and Kelvin probe force microscopy (KPFM). Additionally, the structure representation of the suspended 2D InSe-based device is also depicted. In Fig. 1b, the height profile shows that the InSe nanosheet exists a thickness of approximately 11.8 nm (∽ 16 layers). The 3D morphologic map depicts the natural suspension forms for InSe channel with a channel length of approximately 1 μm and the bending depth of around 83 nm, which is smaller than Ni/Au thickness (∽ 152 nm, Supplemental Figure S1). It means the S-InSe sheet does not touch the bottom. Fig. 1c illustrates the typical Raman spectrum of few-layered InSe sheet. According to the group theory (point group: C_{3v}), the peaks nearby 115, 178, 199, and 228 cm^{-1} originate from the vibration modes of $A_1'(\Gamma_1^2)$, $E'(\Gamma_1^2)$-TO, $A_2''(\Gamma_1^1)$-LO, and $A_1'(\Gamma_1^3)$, respectively. [12] The Raman peaks are consistent with previous Raman studies on bulk γ-rhombohedral InSe crystals. The illustration provides a display of the corresponding lattice vibrations. Relevant studies have shown that all phonon modes of multilayer γ-InSe lamellae show red shift upon tensile strain. [13,14]

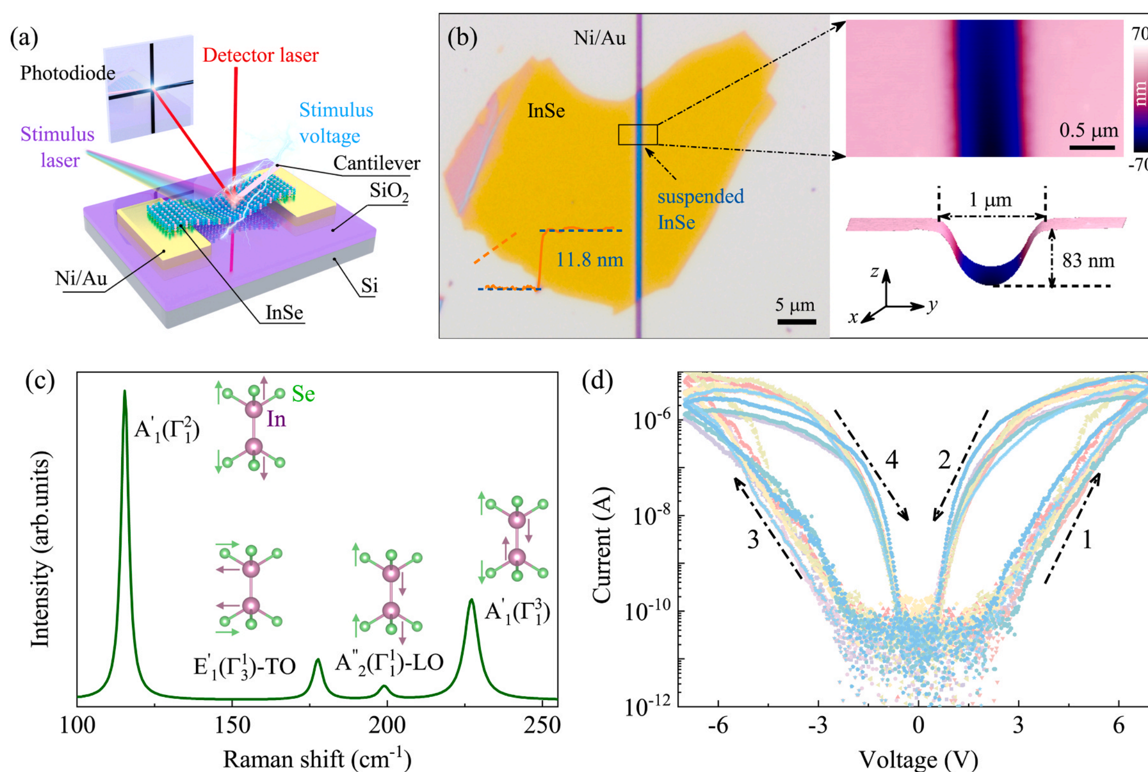

Fig. 1. Structure and electrical behavior of suspended InSe-based memristors. (a) Experimental schematic of a *in-situ* AFM measurement system on the S-InSe device. (b) An optical microscopic image of a S-InSe memristor and the height profile (left panel). The surface morphology and 3D AFM topography of the S-InSe channel (right panel). (c) A Raman spectrum and the mode assignments of a InSe nanosheet. (d) Resistive switching characteristics of ten S-InSe based memristors.

The Raman spectra of S-InSe and F-InSe are shown in the Supplemental Figure S2. Compared with F-InSe, the phonon modes of S-InSe show a red-shifted trend due to the tensile strain. Among them, the peak shift of the E′ mode is the largest, about 0.53 cm^{-1}. This is because the E′ mode is more sensitive to tensile strain than other phonon modes.

In Fig. 1d, a huge volatile resistance switching characteristic with a large current ON/OFF ratio of about 10^5 is observed in S-InSe based devices. As V_{DS} undergoes positive sweeps ranging from 0 V to 7 V and back to 0 V, the channel resistance shifts from a high-resistance state (HRS) to a low-resistance state (LRS). When V_{DS} sweeping negatively (0 V → - 7 V → 0 V), a comparable conversion trend from HRS to LRS is observed. Furthermore, the current-voltage (I-V) characteristics of 36 other S-InSe based show large analog switching feature (Supplemental Figure S3), suggesting a high yield (97 %) of S-InSe based memristors, providing further confirmation of the reliability of large hysteresis behavior observed in these devices. Among them, the standard for determining the working of the device is that the ON/OFF ratio is approximately 10^4 to 10^5, and the hysteresis window is around 10^3.

In order to better compare the differences in I-V characteristics between flat and suspended devices, we fabricated flat devices of which central channel is not suspended against substrate but exhibits bending between the contact electrodes. Channel widths are 1, 3, and 6 μm. The left panel of the Supplemental Figure S4 presents the optical microscopic image of the flat devices, and the right panel shows the I-V characteristic curves corresponding to the flat devices at different channel widths. When scanning back-and-forth in the − 7 ∽ 7 V voltage range, the flat multilayer InSe device displays very small hysteresis, and the memristive behavior could be ignored. Thus, compared with flat devices, the stable large resistive switching behavior of S-InSe based devices is associated with flexoelectric polarization induced by non-uniform strain in bent flakes.

The PFM technique could precisely quantify static flexoelectric polarization of an analogue that are considered to be piezoelectric polarization. [15–17]Fig. 2a exhibits PFM amplitude images of a S-InSe flake with the ascending alternating current (AC) drive voltage (V_{AC}) at 0, 2, and 5 V. Line profiles of Fig. 2a is shown in Supplemental Figure S5. When no drive voltage is applied, the piezoelectric response mapping of the flat and suspended regions is the same. The piezoresponse amplitude between the F-InSe and S-InSe sheets is significantly under non-zero driving voltage. Apparently, with the increasing of the driving voltage, the amplitude of piezoresponse of the suspended area gradually increases, while that of the flat area nearly unchanged.

This phenomenon implies that the amplitude signal does not derive from the intrinsic piezoelectric effect of InSe flakes, but instead from the flexoelectricity arising from the strain gradient. [15] The effective out-of-plane piezoelectric coefficient (d_{33}^{eff}) could further reflect the degree of polarization, which is defined as: [18]$d_{33}^{eff} = \frac{A_P}{V_{AC}}$, where A_P is the driven piezoelectric response displacement. According to the formula, the d_{33}^{eff} coefficient is the slope of linearly fitted curves, as displayed in Fig. 2b. The d_{33}^{eff} coefficient at the center of the InSe channel exhibits a maximum value about 9.6 pm V^{-1}, which significantly surpasses the intrinsic in-plane piezoelectric coefficient ($d_{11} = 1.98$ pm V^{-1}) of InSe flakes. [19] The cross section of bent 2D materials can be approximated as a circular arc. [20] Obviously, the projection in the z direction of intrinsic in-plane piezoelectric coefficient is zero at the center and maximized at the endpoint. In our experiment, the depth and width of the bent-InSe channel are about 83 nm and 1 μm, respectively. Through rough calculation, the maximum projection value of the d_{11} coefficient in the z direction is about 0.592 pm V^{-1}. This value is negligible compared to the d_{33}^{eff} coefficient (about 7.7 pm V^{-1}) obtained at the edge of the curved InSe channel region. It indicates that the d_{33}^{eff} coefficient of S-InSe mainly comes from the flexoelectric effect. In Fig. 2c, the distribution of d_{33}^{eff} coefficients across the S-InSe channel decreases almost symmetrically, reflecting that the flexoelectric polarization also presents a symmetrical distribution in the S-InSe sheet. Therefore, the flexoelectric polarization in bent InSe flake is the main reason for the huge resistive switching behavior of the S-InSe based memristors.

Fig. 3a presents a form-free switching behavior that is set to a LRS in both positive and negative sweeps at high voltage bias (± 4, ± 5, ± 6, and ± 7 V). The device relaxes back to a HRS after voltage removal, indicating a volatile nature in switching mode driven by the horizontal electric field. Fig. 3b depicts the I-V characteristics for 100 consecutive cycles. The results indicate that the device maintains HRS to LRS conversion with high repeatability. In contrast to the memristor based on conductive-filament that affected by random device variability, our devices present good analog switching characteristics with cycle-to-

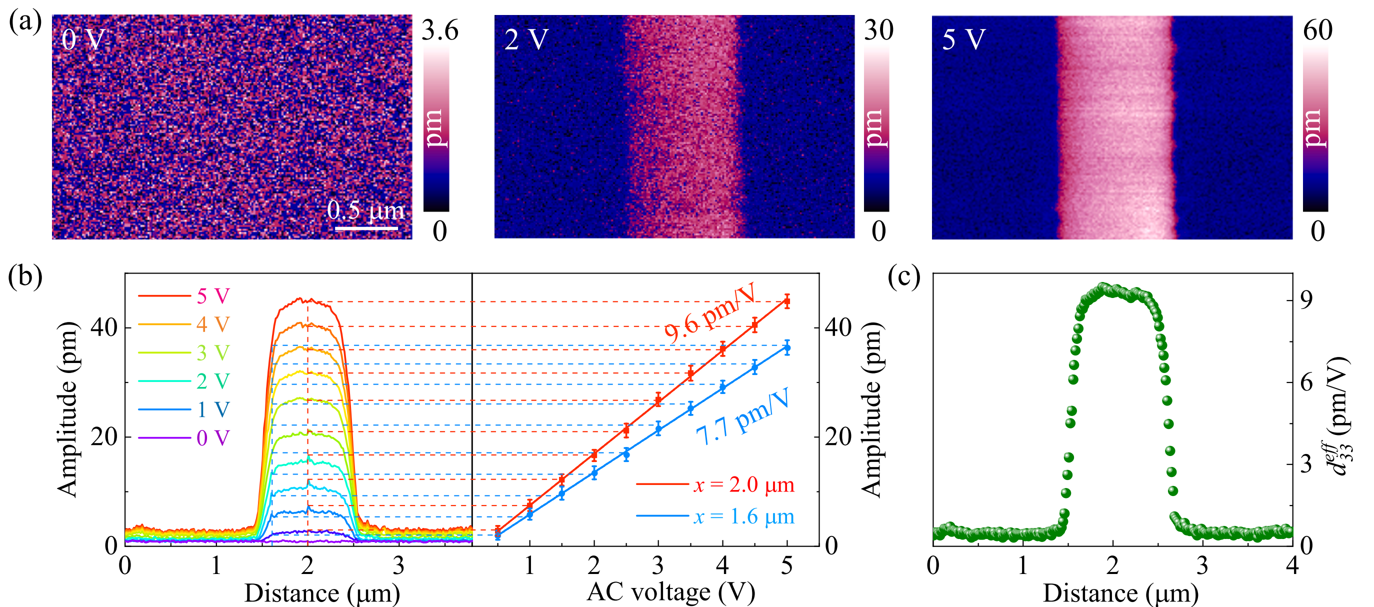

Fig. 2. The PFM measurements of the S-InSe device. (a) Images of the out-of-plane piezoelectric response of the S-InSe channel at 0, 2, and 5 V driving voltages. (b) Statistical distribution of the PFM amplitudes at the driving voltages from 0 V to 5 V (left side) and the corresponding PFM amplitude as a function of AC voltage at x = 1.6 and 2 μm (right side). (c) The d_{33}^{eff} coefficient across the S-InSe channel.

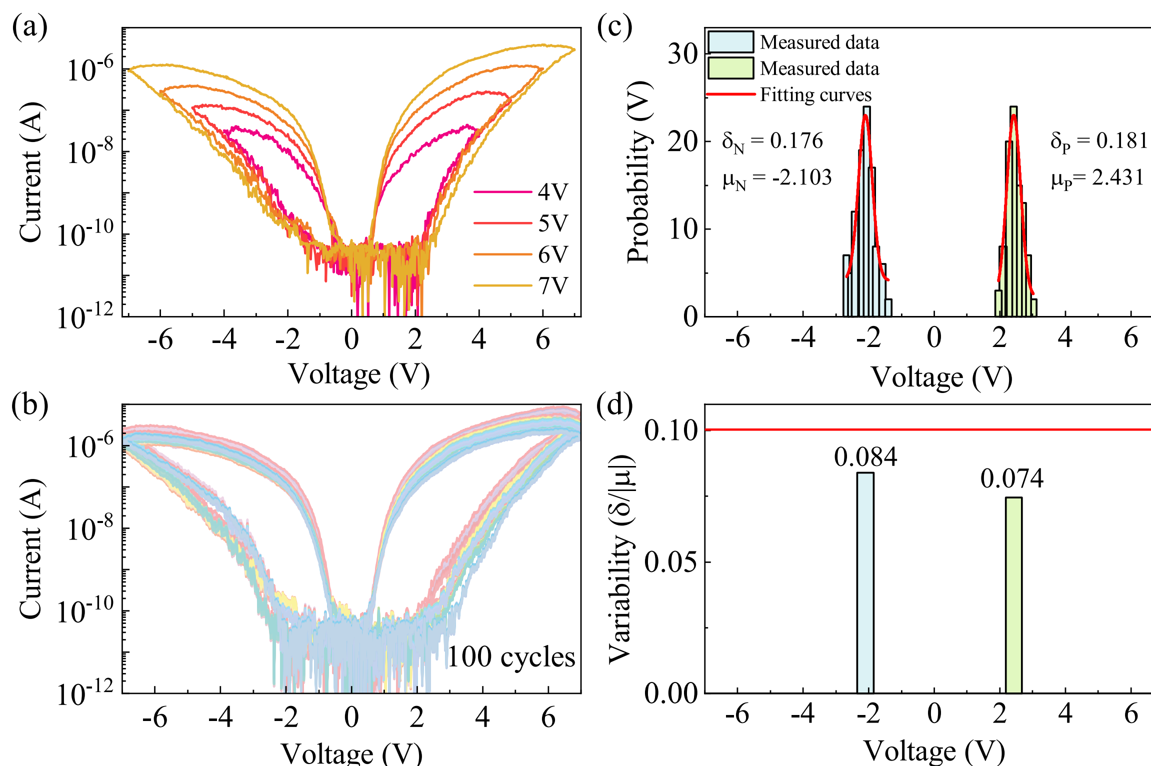

Fig. 3. Horizontal electric field-driven switching characteristics of the S-InSe device. (a) I-V curves of a S-InSe device with various sweep voltages. (b) Repeatable switching I-V characteristics for a S-InSe device. (c) Histogram of the InSe memristor set voltages for negative (blue) and positive (green) sweeps, and the solid lines are fits of the histograms with a Gaussian function. (d) The set voltages variability in the S-InSe based device.

cycle homogeneity. The set voltage histogram for positive and negative sweep is shown in Fig. 3c. It presents a narrow distribution of set voltage around $\pm$ 2.2 V and a low degree of temporal variability. Through fitting the set voltage histograms with the Gaussian curves, the variabilities of the positive/negative set voltages (defined as $\delta/|\mu|$, δ is the standard deviation, and μ is the mean of the set voltage) are obtained to be 0.074 and 0.084, respectively, as presented in Fig. 3d.

The volatile memristive mechanism

An *in situ* KPFM is used to investigate the switching mechanism of the volatile memristor due to the horizontal device architecture. Local surface potential maps of S-InSe based devices can be provided by KPFM images. [20] In actuality, the measurement of surface potential via KPFM is the contact potential difference (CPD) that exists between the sample surface and the tip. The contact potential difference (V_{CPD}) can be written as $V_{CPD} = \frac{\phi_{tip} - \phi_{sample}}{e}$, where e is the elementary charge, ϕ_{sample} is the work function of the sample, and ϕ_{tip} is the work function of the tip. Since the work function of the tip is the same during the measurement, a larger work function means a smaller surface potential. In Fig. 4a, upon initial state, the surface potential in the S-InSe region is observed to be obviously lower than that at the F-InSe region. This indicates the formation of a potential well. It indicates a greater contact barrier in the case of the HRS state. The S-InSe region exhibits a higher work function than the F-InSe region, resulting in a redistribution of charge.

The flat *n*-type InSe flake exhibits an evenly distributed charge carriers, indicating a flat band structure (Supplemental Figure S6a). The bands of S-InSe films suspended on the channel are rearranged under the influence of non-uniform strain. Under the positive strain, the conduction band minimum (CBM) and the valence band maximum (VBM) gradually move upward. However, with the application of negative strain, the CBM and VBM gradually move downward. [21] In S-InSe-based devices, the symmetrical curvature of the S-InSe channel produces a positive strain at the point of symmetry. The presence of positive strain induces both the VBM and CBM of S-InSe to shift upward. Thus, as shown in Fig. 4a, two symmetric intramolecular heterojunctions with type II band alignment are formed. Obviously, the carriers will diffuse and reach equilibrium. The charge redistribution occurs with the flexoelectric polarization. As the net negative charges amasses in the central region, depletion zones are formed on both flanks, forming built-in electric fields on both the left and right sides pointing to the center region (E_1: the built-in electric field pointing right; E_2: the built-in electric field pointing left), as shown in Supplemental Figure S6b. Therefore, the energy band of the S-InSe film is curved upward, and the work function of F-InSe is smaller than that of S-InSe. This conclusion is agree well with KPFM test results of the suspended InSe-based device in the initial state.

In order to exclude the CPD difference between F- and S-InSe induced by doping of the bottom electrode, we prepared F-InSe devices on the bottom electrodes of different metals (Ag, Cu), as shown in the left panel of the Supplemental Figure S7. Among them, the width of the channel is 1 μm. The InSe flakes with the same bending state (68 nm) were selected for KPFM testing, as shown in the right panel of the Supplemental Figure S7. It can be found that the InSe sheets with the same bending state have similar band bending on different bottom metal electrodes, and the difference in CPD between F- and S-InSe is consistent. Therefore, the bottom electrode is undoped with InSe. The difference in CPD between F- and S-InSe is induced by the flexoelectric effect.

In addition, we further clarified the relationship the band bending and morphology of the suspended region, as shown in the Supplemental Figures S8–10. The degree of band bending can be further expressed by the difference in CPD between F- and S-InSe. The greater the band bending, the more obvious the CPD difference between F- and S-InSe. When the InSe sheet with a thickness of 10 nm is suspended on a channel of near 1 μm, the deeper the bending depth, the greater the band bending, as presented in the Supplemental Figure S8. The right panel of

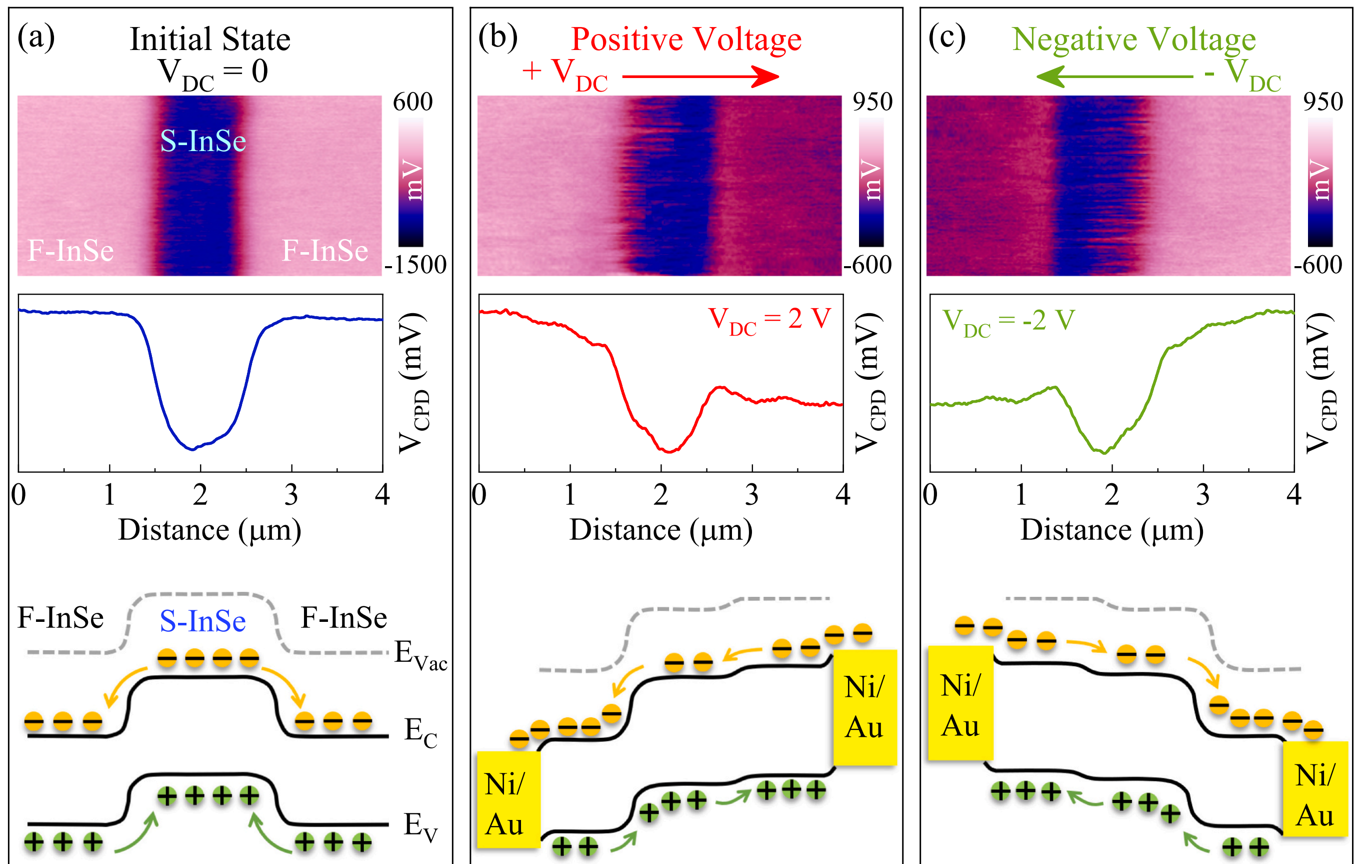

Fig. 4. *In situ* KPFM measurement of the memristive mechanism. KPFM images (top panel), surface potential distribution across the channel (middle panel), and the corresponding schematic diagram of dynamic modulation of the contact barrier (bottom panel) of a InSe-based device at various voltage states of (a) $V_{DC} = 0$, (b) $+ V_{DC}$, and (c) $- V_{DC}$.

the Supplemental Figure S9 presents the surface potential distribution of InSe sheets with a bending depth of 45 nm and a thickness about 10 nm suspended on channels of different widths. The left panel is the corresponding scan height map along the channel. It can be found that the wider the channel, the smaller the band bend. When InSe sheets of varying thicknesses (17 nm and 27 nm) with bending depths of 40 nm are suspended on channels of about 1 μm, the thicker the thickness, the smaller the band bends, as shown in the Supplemental Figure S10. Therefore, the band bending is related to the degree of strain experienced in the suspension region. The larger the strain in the suspended region, the more the VBM and CBM move upward,[21] resulting in greater band bending.

Figure 4b shows the local surface potential of the InSe device when a positive direct current voltage ($+ V_{DC}$) is applied. The barrier on the left side of the channel is increased while that on the right side is decreased. The variation in barriers originates from the dynamic tuning of the built-in electric fields. Under the circumstance of applying $+ V_{DC}$ to the right, the external bias is in the same direction as the built-in electric field E_1 and opposite to E_2. At this point, E_1 is enhanced and E_2 is weakened compared to the initial state. Thus, the left side of the channel presents a strengthened barrier, while the right side displays a reduced one. It's reverse for the case of applying a negative direct current voltage ($- V_{DC}$), as depicted in Fig. 4c. Therefore, the dynamic modulation of the external V_{DC} to the barrier of the S-InSe device is the main reason for the memristive behavior.

The rectification-mediated switching behavior driven by a direct current bias can be used to describe the switching process of the suspended InSe-based devices. [22] The applied V_{DC} voltage gradually modifies the degree of rectification of the device during the rectification-mediated switching. The degree of rectification refers to the forward/backward current ratio of the memristor at a given voltage. A qualitative device model is proposed to describe such a switching behavior, as illustrated in Fig. 5. In this particular model, the S-InSe based memristor displays a symmetrical small-signal I-V characteristic due to its symmetrical diode/S-InSe/diode structure, as presented in Fig. 5a. We defined the analytical I-V characteristic obtained over a voltage range that is relatively small well below the threshold as "Small signal I-V". It can be used as a property of the transport state of the memristor that can be utilized to represent its instantaneous conductance state. When a positive voltage ($+ V_{DC}$) is applied, there is an increase of the rectification degree and the barrier of the left S-/F-InSe diode, while those of the right diode decreases. The revised rectification degrees for two diodes have been highlighted in different sizes, as illustrated in Fig. 5b. It presents a corresponding croquis of the small-signal I-V characteristics. This memristive condition is defined as the "forward-diode state". On the contrary, Fig. 5c displays the condition of negative voltage ($- V_{DC}$), in which the degrees of rectification of the right and left S-/F-InSe diodes are enhanced and reduced, respectively. We refer to this state as the "backward-diode state". The anticipated DC-programmed switching characteristic profile is obtained from the proposed device model, as shown in Fig. 5d. This switching behavior is well in agreement with the experimentally observed rectification-mediated properties in S-InSe based memristors (Fig. 1d).

In addition, we explain in more detail the origin of the hysteresis phenomenon in the I-V curve based on the band diagram. We assume that when the voltage is M V, the corresponding current is I_B in the forward sweep (O → B → C) and I_A in the negative sweep (C → A → O), as shown in the Fig. 5. During the scanning of B → C → A, a positive electric field greater than M V is applied to the S-InSe device all the time. In this case, the external bias is in the same direction as the built-in electric field

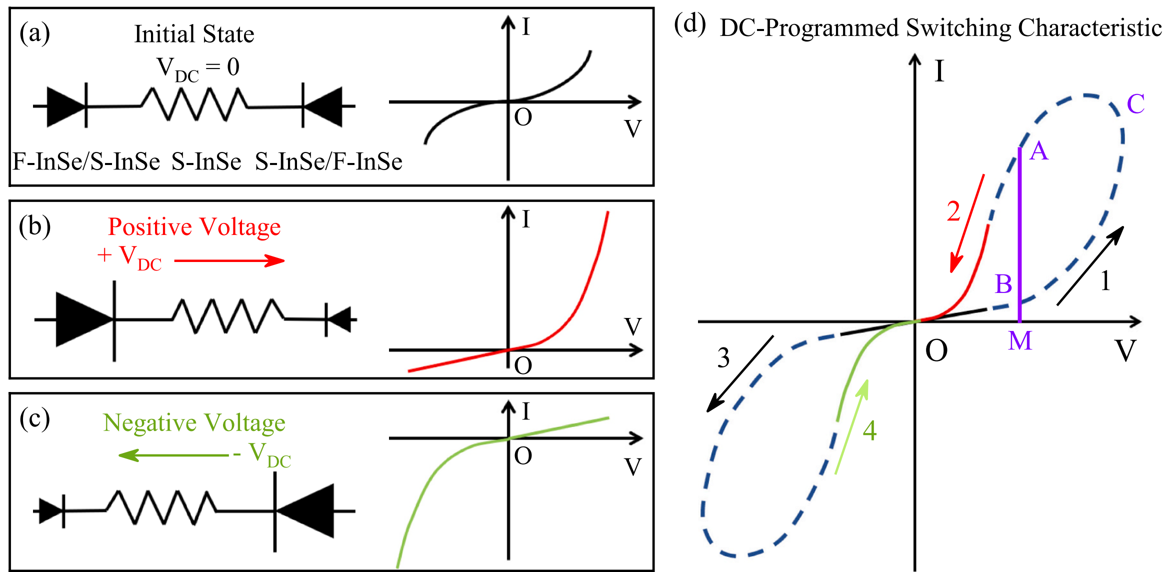

Fig. 5. A qualitative device model for the rectification-mediated DC program-controlled switching processes of the suspended InSe-based memristors. The process involves three memristive states and the corresponding small-signal I-V characteristics: (a) initial state, (b) forward-diode state, and (c) backward-diode state. In this proposed model, the F-InSe is depicted as two diodes in opposite directions sandwiched in the S-InSe channel. (d) Anticipated DC-programmed switching characteristic curve. The small I-V characteristics of backward-diode and forward-diode states are shown by the green solid line and red solid line, respectively. The switching process between the two states is represented by the dashed line. When the voltage is M V, the intersection points with the DC-programmed switch characteristic curve during the forward and negative sweeps are B and A, respectively. Point C is the end point of the right edge of the curve.

E_1 and opposite to E_2. In the band diagram below the Fig. 4b, the barrier on the left side of the channel further increases, while the barrier on the right side further weakened. Under the circumstances, the band structure is more conducive to the migration of electrons. Therefore, during the continuous scanning of B → C → A, the number of carriers in the loop shows a continuous increasing trend. When the voltage returns to M V again during the negative sweep, the number of carriers present in the loop is larger, so I_A is greater than I_B. Therefore, I-V curve show hysteresis during the continuous scanning of the bias voltage.

Multi-field perceptual artificial nociceptors

The threshold switching and relaxation feature of the volatile memristor bear a resemblance to the biological counterpart, providing a good candidate for artificial nociceptor. Here, we fabricated a multi-field perceptual nociceptor based on the S-InSe based memristor. Voltage and light pulses are applied to simulate the common behavior of nociceptors under the tactile and visual systems. Fig. 6a displays the working principle of nociceptors and the analogy of the biological counterpart. Biological nociceptor is triggered by strong noxious stimulus (suprathreshold) that could potentially injure tissues. [23–25] The noxious signals (chemical molecules, mechanical stress, extreme temperatures, etc.) picked up from free nerve endings will be incorporated and transferred through the spinal cord (central nervous system) to the brain, producing a reflexive exit from the noxious stimuli and a sense of pain to prevent further exposure to such stimuli.

In the as-presented memristors, voltage pulses are applied to simulate the external stimuli. For artificial nociceptors, the trigger mechanism depends on the magnitude and time of duration of the input voltage pulse. In order to induce an active state of artificial nociceptors, input pulses with varying amplitudes (A_p) and widths (W) are utilized as external stimuli. Remarkably, the resting period between each test is sufficiently long (10 min), enabling the full recovery of HRS in the volatile memory. Under single-shot voltage pulses with the duration of 2 s, the memristor remains in the OFF state until an input pulse of 10 V is applied, at which point the current will exceed the pain threshold ($I_{nox} = 2\,\mu A$), as shown in Fig. 6b. The output current increases steadily with an escalating input stimulus, which aligns with a stronger pain index in a sensory nociceptor triggered by a higher-intensity noxious stimulus. In Fig. 6c, various pulse widths (W: 0.1 s ∽ 3 s) and a fixed stimulus amplitude of 7 V are also administered to the artificial device. It turns ON once the pulse width exceeds 3 s, and the output current rises with further heightening of the pulse width, indicating the heightened sensitization of the nociceptor device to the prolonged noxious stimulus. This phenomenon agrees well with the fact that the neural system cannot perceive pain from short-term external damage for a transient period of time. In addition, we present the voltage input pulses corresponding to Fig. 6b and c in Supplemental Figure S11 to show the delay. The delay time for the device to respond to external stimuli is very short and almost non-existent. However, if the noxious stimulus duration is continually increased, the non-painful response turns into a pain-perception event. [26] In order to establish with certainty whether the nociceptor is evoked or not, Fig. 6d and Supplemental Figure S12 present a 3D image of the current reaction to input pulses with varying magnitudes and durations. It exhibits typical non-painful behavior characteristics when stimuli are below the threshold plane, while it displays pronounced pain perception when the external stimuli exceed the threshold plane.

In cases where multiple voltage pulses are used, the output current is heavily relies on the pulse amplitude and accumulated time. Fig. 6e depicts the current response of devices to continuous multiple pulses (W: 2 s; interval Δt: 0.5 s) with various amplitudes ($A_p = 5$, 7, and 10 V). The device remains in a HRS state after a series of 15 voltage input pulses of 5 V and 2 s. As the pulse amplitude increases to 7 V and 10 V, the output current exceeds the nociceptive threshold at the 8th and 1st input pulse, and higher current levels are reached (Supplemental Figure S13). The results present that the threshold characteristics of the memristive nociceptor is strongly correlated with the pulse amplitude. To be more precise, activating the nociceptor requires a large number of low-intensity input pulses. Notably, as soon as the target current is reached, the device will maintain high-conductance states by applying an extra amount of voltage pulses. It suggests that the pain intensity is fairly stable with negligible current fluctuations when repeatedly inputting the same superthreshold stimuli.

In damaged tissues, the state of sensitized of nociceptors is evoked to enhance pain sensitivity to extrinsic stimuli, leading to neuropathic

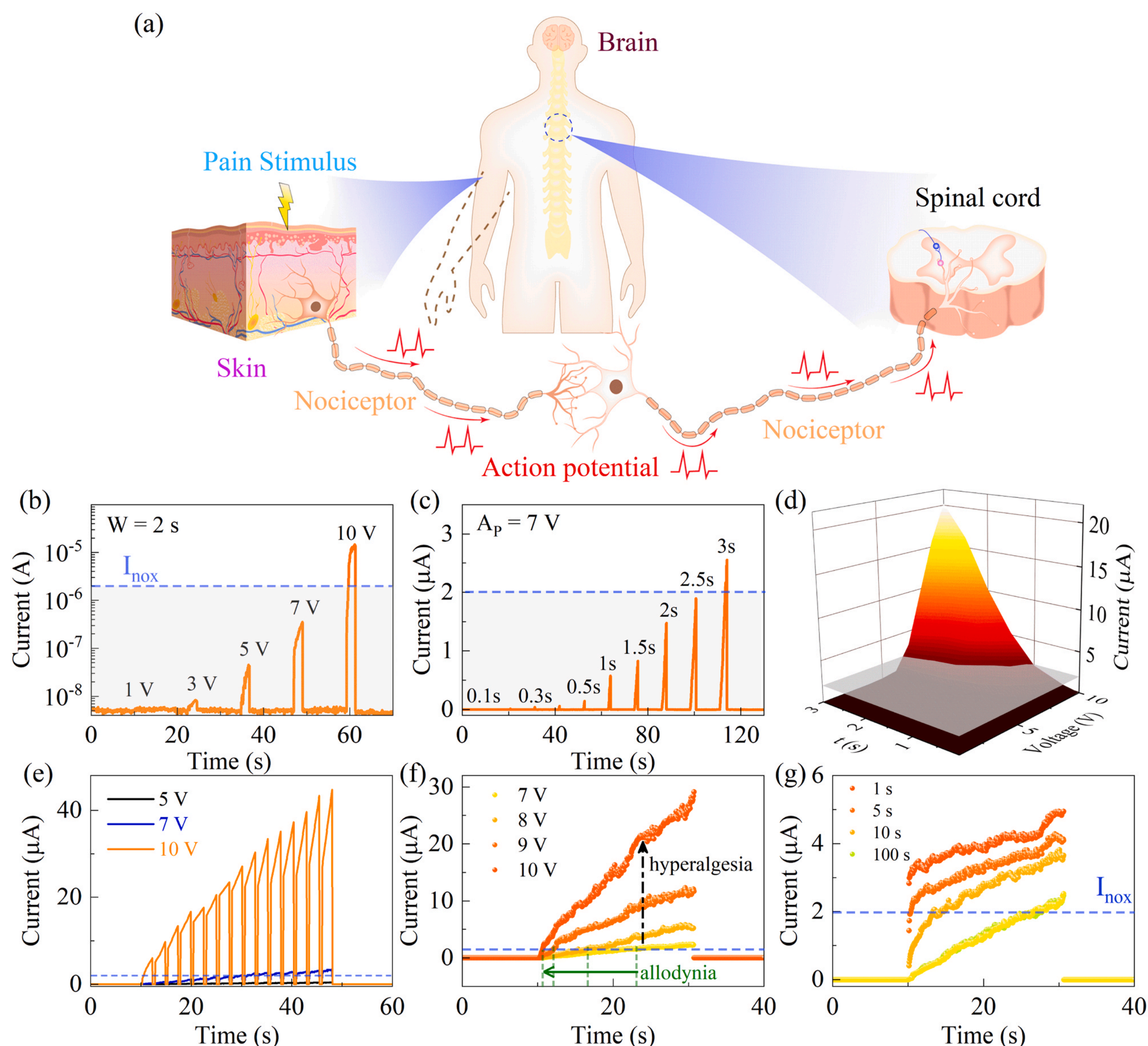

Fig. 6. Voltage pulse responses of the suspended InSe-based memristor for mimicking common behaviors of the typical biological nociceptor. (a) A schematic image of the typical biological nociceptor perceiving noxious stimuli in the neural system of a human body. (b) Current responses over a series of 2 s wide voltage pulses with various amplitudes (1 – 10 V). Pain threshold current I_{nox} is 2 μA. (c) Current responses triggered by voltage spikes with various pulse durations of 0.1 – 3 s at 7 V. (d) A 3D image of the current as functions of voltage pulse amplitude and duration. Threshold plane: 2 μA. (e) Current response of a device to continuous multiple pulses (pulse duration: 2 s; interval: 0.5 s) with different amplitudes (5, 7, and 10 V). (f) Current response after various injuries (8, 9, and 10 V). The current at 7 V is recorded as the normal state. (g) The injured state of the memristor is induced using a noxious stimulus, and then pain assessment (current response is assessed again at 7 V. A self-healing procedure of the wounded tissue is simulated by the fading switching dynamics.

pain-a lower threshold for pain activation (allodynia) and an enhancement in the reactive pain index (hyperalgesia). Firstly, high magnitude input voltage pulses ($A_p = 8$, 9, and 10 V) are used to induce a significant change similar to a tissue damage of the memristor. The current response at the input voltage ($A_p = 7$ V) is recorded as a normal state. Subsequently, the current response to 7 V input voltage is monitored to assess the susceptibility of the impaired system. As displayed in Fig. 6f, the injured nociceptor is more sensitive than the normal case, with higher output currents and faster responses rate. This phenomenon indicates that the artificial nociceptor is characterized by allodynia and hyperalgesia. Furthermore, the fading switching dynamics is used to simulate a self-healing procedure of the wounded organizations. Noxious stimuli ($A_p = 8$ V) are applied to evoke an wounded condition of the memristor, after which pain assessment (current response) is performed again at 7 V normal input after the Δt of 1, 5, 10, and 100 s (Supplemental Figure S14). As shown in Fig. 6g, the wounded state automatically recovers to the regular state within 100 s using the fading property, similar to the self-healing abilityof the biolo gical counterpart. Here, we successfully simulate the common behavior of nociceptors under the haptic system by applying voltage pulses.

In a further step, we triumphantly mimicked common behaviors of the photoexcited corneal nociceptor using light pulses on the S-InSe based memristor, as presented in Fig. 7. The I-V curves of the representative S-InSe device in dark and continuous illumination are shown in the Supplemental Figure S15. When the S-InSe device is positive-biased, the energy level near the left electrode shifts downward, and the closer it is to the electrode, the greater the downward shift. As a result, the left band offset is enhanced, while the right band offset is attenuated or even reversed. The photogenerated carriers are rapidly separated in the opposite direction and extracted by the electrode,

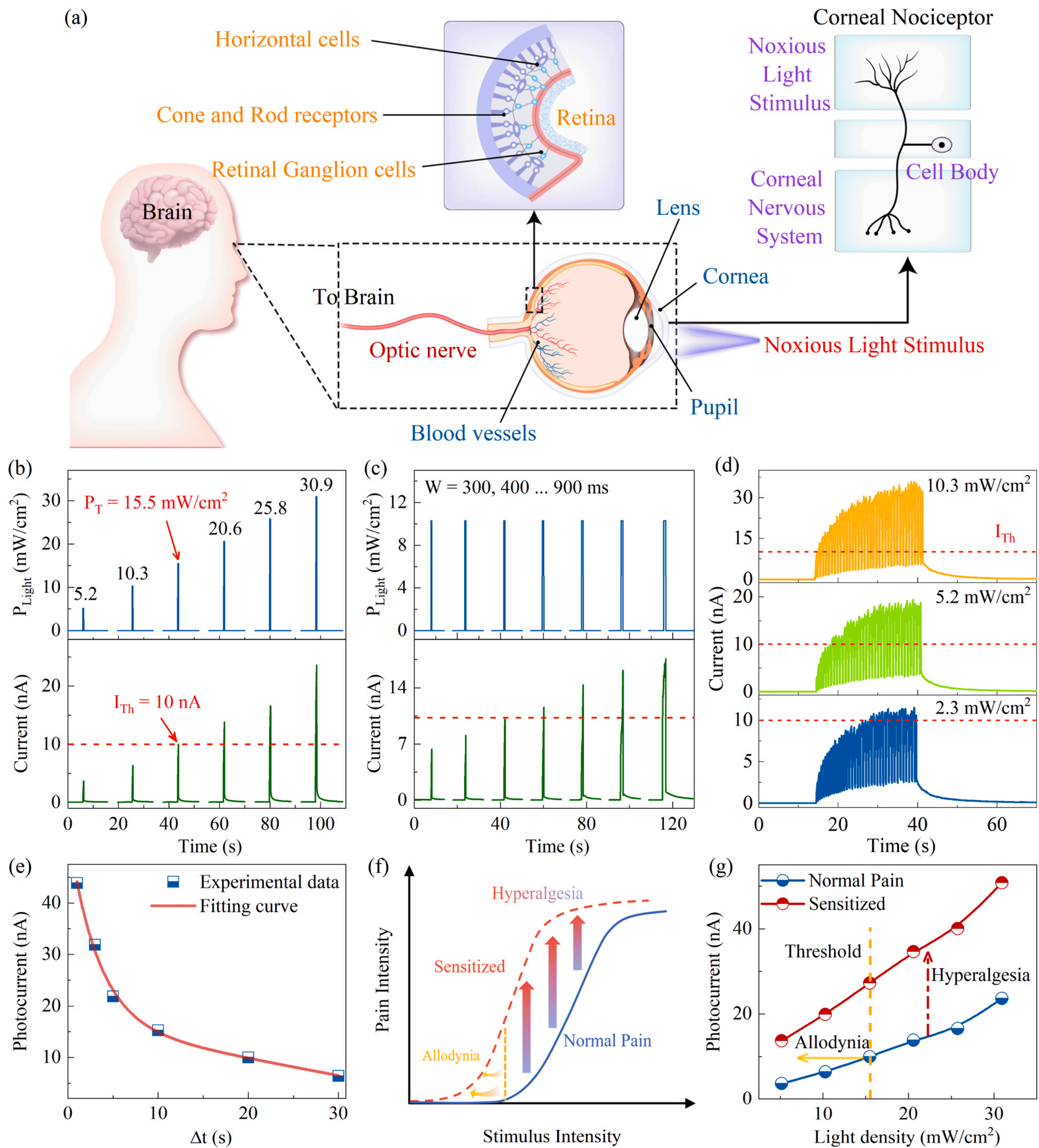

Fig. 7. Light pulse responses of the suspended InSe-based memristor for mimicking common behaviors of the photoexcited corneal nociceptor. (a) The schematic diagrams of human eye receptor and nociceptor system. (b) Photocurrent response of the S-InSe based memristor by applying light pulses with 300 ms width and various pulse amplitudes from 5.2 to 30.9 mW/cm^2. (c) Photocurrent response by applying a fixed light stimulus (10.3 mW/cm^2) with various pulse widths (300 – 900 ms). (d) Current response to continuous multiple laser pulses (W = 300 ms, Δt = 200 ms) with various light intensities (2.3, 5.2, and 10.3 mW/cm^2). (e) At the end of the stimulation group, the photocurrents of the group of detection as a function of interval time Δt. (f) Schematic illustration of the "allodynia" and "hyperalgesia" sensitized characteristics of the nociceptor with growing stimuli intensity in both uninjured and injured conditions. (g) Experimental photocurrents of the memristor preceding and following pulse sequences, showing the appearance of allodynia and hyperalgesia characteristics.

resulting in a high photocurrent. In addition, since the mobility of electrons in n-type InSe is significantly greater than that of holes, these photoexcited electrons move considerably faster in the channel than photoexcited holes. Over their entire life cycle, these electrons can cycle through the circuit multiple times, resulting in high photoconductive gain.

The visual processing is one of the fundamental and prominent functions of the human brain, which is accomplished through the prominent features of human's eyes. [27] The eye is a natural visual processor and detector, which is composed of a multitude of nociceptors and receptors. Of all categories of nociceptors, photoexcited corneal nociceptor (PCN) stands as the first line of protection that protects the

eye against harmful light stimuli and safeguards eyes against any possible risks. Fig. 7a illustrates the PCN operating principle. Corneal cells will release endogenous chemical mediators when harmful light stimuli reach the cornea. Subsequently, electrical signals are generated by the corneal nociceptor fibers triggered by endogenous chemical mediators. The PCN determines whether an action potential is generated by comparing the signal amplitude to its threshold. Once generated, the action potential is delivered to the brain through the central nervous system. The corneal nociceptor is activated under the circumstance of a higher signal level than the threshold, and then transmits the pain signal to the central nervous system, inducing reactions like tears and pain.

The occurrence of PCN in biological systems greatly depends to a large extent on the duration width, magnitude and aggregate amount of harmful light stimuli in the outside environment. [28] Hence, laser pulses with various amplitudes (P), widths, intervals, and counts are applied on the S-InSe channel to simulate the external stimulation of nociceptors. The photocurrent amplitude of the S-InSe channel is considered to be the response of the PCN to external stimuli. Note that the photocurrent amplitude of 10 nA is referred to as the "threshold line" (I_{TH}) of the PCN. That is to say, the PCN is "activated" and initiates the warning program once the photocurrent reaches/surpasses the I_{TH}. Fig. 7b exhibits that the device photocurrent does not exceed the threshold line until the light power reaches 15.5 mW/cm^2, which is referred to as the triggered-threshold power (P_T). The pulse power above P_T is regarded as effective (invalid) stimuli. With increasing the laser pulse power, the photocurrent amplitude increases steadily. The result is similar to the triggering behavior of PCN: the PCN response intensity grew with the higher intensity of the harmful light stimulus, and the nociception generated by the central nervous system is more pronounced. Fig. 7c shows that a longer pulse width results in a larger output current. This phenomenon is similar to a biological procedure: the PCN is irritated when it is stimulated for a brief period of time by a mildly harmful light stimulus, it is not activated, at which point the central nervous system fails to detect the pain signal. With increasing the duration of stimulation, the PCN is excited and the central nervous system reacts to the pain signals, which in turn produces painful feeling. In Fig. 7d, the device cannot be "activated" at each power of a single laser pulse (ineffective stimulus), while the photocurrent amplitude gradually rises above the threshold line as the number of laser pulses increases. In addition, the time needed to reach the threshold line becomes shorter with increasing light power. This is analogous to PCN behavior in which continuous exposure to a mild noxious stimulus could also trigger activation of the PCN response. The photocurrent enhances with the raising pulse number after exceeding the threshold line, without any relaxation and attenuation. The results present that the PCN has the feature of "no-adaptation", which is an essential function for the protection of the visual system.

The relaxation property is another important behavior of PCN to further reinforce the eye protection from secondary injuries. [29] The PCN moves into the relaxation period after removal of the noxious light stimulus, at which time the noxious light stimulus lower than the threshold of triggered will also re-activate the PCN. That is to say, even a slight noxious stimulus produces more painful feeling before the preceding pain is fully gone. The photocurrent nicely mimics the relaxation characteristic of PCN (Supplemental Figure S16). Fig. 7e exhibits that the photocurrent triggered by the inspection set has a time-dependent relaxation property. It declines with increasing the time interval. The excitability falls below the threshold line if the interval time is prolonged sufficient. Otherwise, the photocurrent response induced by the detection cluster still "activate" the device, producing a noticeable "pain".

Furthermore, the main feature of the PCN is to exhibit "allodynia" and "hyperalgesia" behaviors. In the case of the eye exposed to intense ultraviolet light, the cornea will be painful and develop photokeratitis. Following cornea injured, inflammatory mediators produced by wounded corneal cells motivate the PCN to shorten the threshold (allodynia) while increasing the response intensity (hyperalgesia), as indicated by the arrows in Fig. 7f. Here, the application of sequence of 20 light pulses (P = 15.5 mW/cm^2, W = 300 ms, Δt = 200 ms) to the S-InSe channel is used to simulate the wounded condition (Supplemental Figure S17). The photocurrents of the individual laser pulse of varying light power preceding (uninjured state) and following (injured state) the pulse sequence are represented by the blue and red lines in Fig. 7g, respectively. In the "uninjured" state (pre-pulse trains), the device response enhances with the pulse power. However, in the "injured" state (following the pulse trains), the device displays significantly greater photocurrents over the full range of the application of the laser power. At the same time, the P_T moves to the side that is lower, which indicates that a lesser P_T is required to activate the "injured" device. Therefore, the S-InSe based memristor successfully simulates the hyperalgesia and allodynia properties of the PCN.

Conclusion

In summary, we have novelly proposed a general strategy for constructing lateral memristors based on flexoelectric effect, taking suspended InSe flakes as the representative 2D material. Compared with the SiO_2-supported InSe device, the suspended InSe-based memristor displays remarkable resistive switching characteristics including a large ON/OFF ratio of 10^5, forming-free operation, up to 97 % yield, and 7.4 % cycle-to-cycle variation. The S-InSe region has a significantly reduced surface potential compared to the flat region, which is related to charge redistribution. The deviation of the surface potential between the suspended and flat zones lead to a potential barrier. The dynamic tunable barrier of the S-InSe based device by the external DC bias voltage is the primary reason for the resistive switching characteristics. In a further step, a qualitative device model is proposed for the first time to explain the switching processes of the suspended InSe-based memristor. Finally, key functions of the artificial nociceptors under electric and light fields, including threshold, relaxation, "no adaptation", and sensitization, are successfully simulated. This study promotes the progress of the 2D materials-based lateral memristors, meanwhile providing fresh approaches for bionic medical machines and humanoid robots based on pain-perception abilities.

Materials and methods

Suspended InSe-based device fabrication

Electron beam lithography (EBL, Pioneer Two, Raith) technique was employed to fabricate the patterned substrates on n^+-Si with 280 nm-thick SiO_2. The 2 nm/150 nm Ni/Au electrodes were evaporated via a thermal evaporator. The channel length is designed between 1 ∽ 2 μm. The few-layered InSe flakes were prepared using the mechanical exfoliation method with a blue tape (Shanghai Onway Technology Co., Ltd) from bulk InSe single crystal (SixCarbon technology, Shenzhen), and then transferred onto electrodes with an accurate transfer platform (Metatest, E1-T). After dry transfer, the layered InSe flakes were suspended within a space between the electrodes, forming a suspended atomic layered structure.

Flexoelectric polarization measurements

The commercial atomic force microscopy (AFM) system (Dimension Icon, Bruker) were used to measure the surface topography and thickness of bent InSe nanosheets. The piezoelectric response is detected through PFM in the contact mode by means of a conductive "SCM-PIT" tip with a Pt/Ir coating. The "SCM-PIT" tip exhibits a tip radius of approximately 20 nm, a resonant frequency of around 75 kHz, and a force constant about 2.8 N/m. In PFM measurements, in order to effectively avoid the contact resonance, the V_{AC} frequency was set to 15 kHz. PFM tests of the bent InSe channel were performed at different

drive voltages, where $V_{AC} = V_{DC} + V_0\cos(\omega t)$. V_0 is the ascending drive voltage, V_{AC} and V_{DC} are the magnitude of the applied alternating current and direct current drive voltage, respectively.

Measurements of in situ KPFM

In-situ switching procedure of the suspended InSe-based memristors was explored by a 2400 digital source meter unit combined with the *Peak-Force* based KPFM system (Dimension Icon, Bruker). We set the drive routing at the tip. The rate is 0.6 Hz and the lift scan height is 60 nm. Connected the memory cell to the 2400 digital source meter unit via a copper strip that was conductive. The voltage was biased at a constant voltage of 2 and − 2 V, respectively. All KPFM images were acquired using a "SCM-PIT" (Bruker) tip.

Artificial nociceptor device measurements

The electronic and photo-electric measurements of the bent InSe-based memristor were carried out at room temperature by the Keithley 4200-SCS semiconductor parameter analyzer in a high-vacuum environment (∽ 10^{-6} Torr). All measurements were taken in dark conditions exposed only to the target light source. A commercial light-emitting diode with an illumination wavelength of 405 nm (Thorlabs, Inc.) was employed for the photo-electric measurements. Utilizing a laser diode or a temperature controller (ITC4001, Thorlabs, Inc.) to control the light pulses with adjustable power intensity, pulse width, and frequency.

CRediT authorship contribution statement

Liangqing Zhu: Methodology. **Yawei Li:** Methodology. **Menghan Deng:** Writing – original draft, Methodology, Investigation, Data curation, Conceptualization. **Li Chen:** Methodology. **Anyang Cui:** Methodology. **Kai Jiang:** Methodology. **Liyan Shang:** Methodology. **Zhigao Hu:** Writing – review & editing, Supervision, Project administration, Funding acquisition, Conceptualization. **Zhaotan Gao:** Methodology, Investigation, Data curation, Conceptualization. **Lin Wang:** Methodology. **Zhangchen Hou:** Methodology. **Xionghu Xu:** Methodology. **Jinzhong Zhang:** Methodology, Funding acquisition, Conceptualization.

Declaration of Competing Interest

The authors declare that they have no known competing financial interests or personal relationships that could have appeared to influence the work reported in this paper.

Data availability

Data will be made available on request.

Acknowledgments

This work was financially supported by the National Natural Science Foundation of China (grant nos. 62090013, 62375086, 62074058, and 12104156), the National Key Research and Development Program of China (grant no. 2019YFB2203403), the Projects of Science and Technology Commission of Shanghai Municipality (grant nos. 21JC1402100 and 23ZR1446400), and the Program for Professor of Special Appointment (Eastern Scholar) at Shanghai Institutions of Higher Learning.

Appendix A. Supporting information

Supplementary data associated with this article can be found in the online version at doi:10.1016/j.nantod.2024.102332.

References

[1] F. Liang, W. Yu, D. An, Q.Y. Yang, X.W. Fu, W. Zhao, IEEE Access 6 (2018) 15132–15154.
[2] H. Duan, S.Q. Cheng, L. Qin, X.L. Zhang, B.Y. Xie, Y. Zhang, W.J. Jie, J. Phys, Chem. Lett. 13 (2022) 7130–7138.
[3] K.H. Liao, P.X. Lei, M.L. Tu, S.W. Luo, T. Jiang, W.J. Jie, J.H. Hao, ACS Appl. Mater. Interfaces 13 (2021) 32606–32623.
[4] W. Huh, D. Lee, C.H. Lee, Adv. Mater. 32 (2020) 2002092.
[5] H. Yang, J. Heo, S. Park, H.J. Song, D.H. Seo, K.E. Byun, P. Kim, I. Yoo, H.J. Chung, K. Kim, Science 336 (2012) 1140–1143.
[6] V.K. Sangwan, D. Jariwala, I.S. Kim, K.S. Chen, T.J. Marks, L.J. Lauhon, M. C. Hersam, Nat. Nanotechnol. 10 (2015) 403–406.
[7] V.K. Sangwan, H.S. Lee, H. Bergeron, I. Balla, M.E. Beck, K.S. Chen, M.C. Hersam, Nature 554 (2018) 500–504.
[8] R.H. Dennard, F.H. Gaensslen, Y. Hwa-Nien, V.L. Rideout, E. Bassous, A.R. LeBlanc, IEEE J. Solid State Circuits 9 (1974) 256–268.
[9] X.J. Zhu, D. Li, X.G. Liang, W.D. Lu, Nat. Mater. 18 (2019) 141–148.
[10] M. Yoshida, R. Suzuki, Y.J. Zhang, M. Nakano, Y. Iwasa, Sci. Adv. 1 (2015) 1–7.
[11] D.A. Bandurin, A.V. Tyurnina, G.L. Yu, A. Mishchenko, V. Zlyomi, S.V. Morozov, R. K. Kumar, R.V. Gorbachev, Z.R. Kudrynskyi, S. Pezzini, Z.D. Kovalyuk, U. Zeitler, K.S. Novoselov, A. Patan, L. Eaves, I.V. Grigorieva, V.I. Fal'ko, A.K. Geim, Y. Cao, Nat. Nanotechnol. 12 (2016) 223–227.
[12] S. Lei, L. Ge, S. Najmaei, A. George, R. Kappera, J. Lou, M. Chhowalla, H. Yamaguchi, G. Gupta, R. Vajtai, A.D. Mohite, P.M. Ajayan, ACS Nano 8 (2014) 1263–1272.
[13] Z.B. Huangfu, J.B. Wang, X.R. Cheng, S.Q. Feng, Y.F. Liang, C.S. Yuan, X. Zhu, Z. Wang, H.J. Zhang, K. Yang, J. Alloy. Compd. 961 (2023) 170998.
[14] C.Y. Song, F.R. Fan, N.N. Xuan, S.Y. Huang, C. Wang, G.W. Zhang, F.J. Wang, Q. X. Xing, Y.C. Lei, Z.Z. Sun, H. Wu, H.G. Yan, Phys. Rev. B 99 (2019) 195414.
[15] X. Wang, A.Y. Cui, F.F. Chen, L.P. Xu, Z.G. Hu, K. Jiang, L.Y. Shang, J.H. Chu, Small 15 (2019) 1903106.
[16] C.J. Brennan, R. Ghosh, K. Koul, S.K. Banerjee, N. Lu, E.T. Yu, Nano Lett. 17 (2017) 5464–5471.
[17] M.H. Deng, X. Wang, X.H. Xu, A.Y. Cui, K. Jiang, J.Z. Zhang, L.Q. Zhu, L.Y. Shang, Y.W. Li, Z.G. Hu, J.H. Chu, Mater. Horiz. 10 (2023) 1309–1323.
[18] N. Syed, A. Zavabeti, J.Z. Ou, M. Mohiuddin, N. Pillai, B.J. Carey, B.Y. Zhang, R. S. Datta, A. Jannat, F. Haque, K.A. Messalea, C. Xu, S.P. Russo, C.F. McConville, T. Daeneke, K. Kalantar-Zadeh, Nat. Commun. 9 (2018) 3618.
[19] Y. Guo, S. Zhou, Y.Z. Bai, J.J. Zhao, Appl. Phys. Lett. 110 (2017) 163102.
[20] X. Wang, X. Zhou, A.Y. Cui, M.H. Deng, X.H. Xu, L.P. Xu, Y. Ye, K. Jiang, L. Y. Shang, L.Q. Zhu, J.Z. Zhang, Y.W. Li, Z.G. Hu, J.H. Chu, Mater. Horiz. 8 (2021) 1985–1997.
[21] M.M. Yang, W. Gao, Q.Q. Song, Y.C. Zhou, L. Huang, Z.Q. Zheng, Y. Zhao, J.D. Yao, J.B. Li, Adv. Opt. Mater. 9 (2021) 2100450.
[22] D. Li, B. Wu, X.J. Zhu, J.T. Wang, B. Ryu, W.D. Lu, W. Lu, X.G. Liang 12 (2018) 9240–9252.
[23] H. Wei, H. Han, K. Guo, H. Yu, J. Gong, M. Ma, Y. Ni, J. Feng, Z. Xu, W. Xu, Mater. Today Phys. 18 (2021) 100329.
[24] R.A. John, N. Yantara, S.E. Ng, M.I. Bin Patdillah, M.R. Kulkarni, N.F. Jamaludin, J. Basu, Ankit, S.G. Mhaisalkar, A. Basu, N. Mathews, Adv. Mater. 33 (2021) 2007851.
[25] F. Wang, S.B. Ma, Z.C. Tian, Y.T. Cui, X.Y. Cong, W.B. Wu, F.D. Wang, Z.Z. Li, W. J. Han, T.Z. Wang, Z.C. Sun, F.L. Zhang, R.G. Xie, S.X. Wu, C. Luo, Pain 162 (2021) 135–151.
[26] H.H. Wei, Y. Ni, L. Sun, H.Y. Yu, J.D. Gong, Y. Du, M.X. Ma, H. Han, W.T. Xu, Nano Energy 81 (2021) 105648.
[27] C.D. Gilbert, W. Li, Nat. Rev. Neurosci. 14 (2013) 350–363.
[28] J.H. Yoon, Z.R. Wang, K.M. Kim, H.Q. Wu, V. Ravichandran, Q.F. Xia, C.S. Hwang, J.J. Yang, Nat. Commun. 9 (2018) 417.
[29] M. Kumar, H.-S. Kim, J. Kim, Adv. Mater. 31 (2019) 1900021.

Menghan Deng received her BS degree from Donghua University in 2019. She is now a Ph.D. student at East China Normal University. Her research interests include the photoelectrical and flexoelectric properties of two-dimensional materials-based devices.

Zhigao Hu is a professor and doctoral supervisor in Department of Physics, School of Physics and Electronic Science, East China Normal University. He was selected as an excellent academic leader of Shanghai in 2014, and a special professor of Shanghai (Oriental Scholar) in 2014. His research interests include Optoelectronic functional materials and micro/nano devices; Two-dimensional semiconductors and electronic devices; Theoretical model of solid state spectroscopy and device designs. He has published over 200 peer-reviewed academic papers.